Modeling of Casting, Welding, and Advanced Solidification Processes - XII
Edited by: Steve L. Cockcroft and Daan M. Maijer
TMS (The Minerals, Metals & Materials Society), 2009

MODELING OF REOXIDATION INCLUSION FORMATION IN STEEL SAND CASTING

A.J. Melendez[1], K.D. Carlson[1], C. Beckermann[1], M.C. Schneider[2]

[1]Dep. Mechanical and Industrial Engineering, University of Iowa, Iowa City, Iowa 52242, USA
[2]MAGMA Giessereitechnologie GmbH, Kackertstrasse 11, D-52072 Aachen, Germany

Abstract

A model is developed that predicts the motion and growth of oxide inclusions during pouring, as well as their final locations on the surface of steel sand castings. Inclusions originate on the melt free surface, and their subsequent growth is controlled by oxygen transfer from the atmosphere. Inclusion motion is modeled in a Lagrangian sense, taking into account drag and buoyancy forces. The inclusion model is implemented in a general-purpose casting simulation code. Parametric studies are performed to investigate the sensitivity of the predictions to various model parameters. The model is validated by comparing the simulation results to measurements made on production steel sand castings. Good overall agreement is obtained.

1. Introduction

The removal of oxide inclusions from the surface of steel sand castings and the subsequent repair of those castings are expensive and time consuming. Reoxidation inclusions, which form when deoxidized steel comes into contact with oxygen during mold filling, make up a substantial portion of the inclusions found in steel castings. Griffin and Bates [1] estimated that 83% of the macro-inclusions found in carbon and low-alloy (C&LA) steel castings are reoxidation inclusions. The primary source of oxygen in reoxidation inclusion formation is air, which contacts the metal stream during pouring as well as the metal free surface in the mold cavity during filling. In an attempt to provide foundry engineers with a tool for eliminating or minimizing inclusion problems, a model has been developed that simulates the motion and growth of reoxidation inclusions during the pouring of C&LA steel castings. The oxide mixture that forms during the pouring of C&LA steel is partially liquid [2], as opposed to the solid oxide films or particles that form during casting of high-alloy steel or light metals. Thus, the present model considers inclusions to be individual particles, rather than part of a film. This inclusion model, which is being developed within a general-purpose casting simulation package [3], provides predictions of the distribution of reoxidation inclusions on the surface of C&LA steel sand castings. This information can be used to help determine whether a given rigging design will lead to inclusion problems before production, and can indicate what effect rigging modifications have on the inclusion distribution. The objective of this study is to perform a comparison between simulated inclusion distributions and inclusion distributions determined from experimental inclusion concentration measurements for two industrial castings.

2. Model Description

The inclusion calculations described in this section are performed as part of a standard casting filling simulation. The filling simulation calculates the velocity and free surface geometry of the melt as a function of time during mold filling. The inclusion model assumes that

the reoxidation inclusions are spherical, characterized by their diameter d_{inc}, as depicted in Fig. 1. The inclusions form and grow on the melt free surface, and they are transported through the mold cavity by melt flow. The inclusion model tracks the inclusions in a Lagrangian sense. The model equations are provided in Table 1, along with values of the parameters and constants used in these equations. Material property values given in the table were evaluated at the pouring temperature. In Table 1, V represents volume, $\boldsymbol{u}$ is velocity, T is temperature, $\boldsymbol{x}$ is position, t is time, and $A_{FS,inc}$ represents the area of the melt free surface that contributes oxide to a growing inclusion. This area is determined by apportioning the total free surface area among all inclusions, weighted by each inclusion's volume. Additional detail regarding the models can be found in references [2] and [4].

Table 1. Equations, properties and constants used to simulate inclusions [4].

Equations	
Inclusion growth: $\partial V_{inc}/\partial t = A_{FS,inc}\beta$, where $\beta = \frac{r_{inc} M_{inc}}{\rho_{inc}} \frac{D_{O_2}}{\delta_{O_2}} \frac{p_{O_2}}{\bar{R}T}$	(1)
Oxygen boundary layer thickness: $\delta_{O_2} = L_c \Big/ \left\{ 2 + 0.6 \left(\lvert \boldsymbol{u}_s \rvert L_c / \nu_a \right)^{1/2} \left(\nu_a / D_{O_2} \right)^{1/3} \right\}$	(2)
Inclusion motion: $\rho_{inc} \frac{d\boldsymbol{u}_{inc}}{dt} = \underbrace{\frac{18\rho_l \nu_l}{d_{inc}^2} (\boldsymbol{u}_l - \boldsymbol{u}_{inc}) \left(1 + 0.15 \mathrm{Re}_{inc}^{0.687}\right)}_{\text{drag}} + \underbrace{(\rho_{inc} - \rho_l)\boldsymbol{g}}_{\text{bouyancy}}$, where $\mathrm{Re}_{inc} = \lvert \boldsymbol{u}_l - \boldsymbol{u}_{inc} \rvert d_{inc} / \nu_l$ and $\boldsymbol{u}_{inc} = d\boldsymbol{x}_{inc}/dt$	(3)

Parameters and Constants	
Quantity	**Value**
Inclusion moles per mole of molecular oxygen (r_{inc})	0.42
Effective molecular weight of inclusions (M_{inc})	149 g/mol
Effective inclusion density (ρ_{inc})	3.23 g/cm^3
Diffusivity of oxygen in air (D_{O_2})	4.56 cm^2/s
Partial pressure of oxygen in air (p_{O_2})	21287.25 Pa
Universal gas constant $(\bar{R})$	8.314×10^6 Pa·cm^3/(mol·K)
Kinematic viscosity of air (ν_a)	3.53 cm^2/s
Density of liquid steel (ρ_l)	6.95 g/cm^3
Kinematic viscosity of liquid steel (ν_l)	0.00648 cm^2/s
Gravitational acceleration $(\lvert \boldsymbol{g} \rvert)$	981 cm/s^2
Nucleation diameter (d_{nuc})	10 μm
Nucleation and agglomeration lengths $(L_{nuc} = L_{agg})$	10 mm
Characteristic free surface length (L_c)	30 mm

Inclusion nucleation occurs on the melt free surface, due to the presence of oxygen. The present model simulates nucleation by searching the free surface at the beginning of each filling time step, and if a localized region of the free surface does not contain any inclusions, then tiny inclusions are added over the region, with a nucleation spacing of L_{nuc}. The initial size of these introduced inclusions, d_{nuc}, is taken as a very small value, such that the initial inclusion volume

added by placing these inclusions on the free surface is negligibly small. During each time step in a filling simulation, new free surface area is created, and some inclusions on existing regions of the free surface may be swept away from the surface by the local flow pattern. Both of these situations create regions of the free surface lacking inclusions, where new inclusions will be nucleated. The total number of inclusions nucleated during a filling simulation, therefore, is a direct function of the free surface evolution and the tendency of the flow to draw inclusions away from the free surface.

The growth of reoxidation inclusions occurs due to the mass transfer of oxygen through the air to the melt-air interface, as indicated by Equation (1) in Table 1. This equation is developed in reference [2]. When an inclusion is on the melt free surface, it grows according to Equations (1) and (2). Equation (2) is the Ranz-Marshall correlation, which models heat and mass transfer for droplets of diameter L_c. Although the metal free surface is generally not made up of droplets, this correlation is used to obtain an estimate of the oxygen boundary layer thickness. In the present context, L_c can be thought of as a characteristic free surface length, such as an effective diameter or length of a portion of the free surface. As a first approximation, L_c is taken as a constant in the present model. Since detailed pouring characteristics such as splashing and (surface) turbulence, which greatly influence the free surface and thus inclusion development, are not accurately modeled by general-purpose casting simulation packages, it makes little sense to implement a more complex model for the oxygen transport at the surface.

As indicated by Equations (1) and (2), the inclusion volume increase at each time step is calculated as a function of the free surface area apportioned to each inclusion, $A_{FS,inc}$, the local melt surface velocity, $\boldsymbol{u}_s$, and the characteristic free surface length, L_c. To better understand the effects on growth of the melt surface velocity and characteristic free surface length, it is useful to apply the present growth model to estimate the total reoxidation inclusion volume that forms during pouring of a steel casting. Summing over all inclusions and assuming, for this estimate only, that the growth coefficient β is constant with time and the same for all inclusions, Equation (1) can be integrated over the pouring time and divided by the total steel volume to yield the total inclusion volume fraction in a casting:

$$g_{inc} = \frac{V_{inc}}{V_s} = \beta \left(\frac{1}{V_s} \int_0^{t_{pour}} A_{FS}\, dt \right) \tag{4}$$

In order to determine the value in parentheses in this equation, filling simulations were performed for three production castings. For all three castings, this value was about 100 s/m. Using this value, and using Equations (1) and (2) to calculate β, the inclusion volume fraction was computed from Equation (4) for a range of characteristic free surface lengths and melt surface velocities. The result of this parametric study is shown in Fig. 2. The four curves in this figure correspond to a reasonable range of melt surface velocities. Note that for small characteristic free surface lengths, these equations predict very large inclusion volume fractions. However, for characteristic lengths between about 20 – 50 mm, the inclusion volume fractions are reasonable (several hundred ppm) over the range of velocities shown. For the present study, a constant characteristic length of L_c = 30 mm was chosen. For a free surface velocity of 1 m/s, this value gives an inclusion volume fraction of about 300 ppm. Fig. 3 illustrates the relationship between the inclusion volume fraction and the ratio of ambient air consumption to total steel volume. For an inclusion volume fraction of 300 ppm, the ambient air volume consumed is about 1.8 times the steel volume, which is reasonable: $1.0V_s$ from the air initially in the mold, plus $0.8V_s$ from air entrained during filling. This indicates that the choice of L_c = 30 mm should produce a

reasonable volume of inclusions.

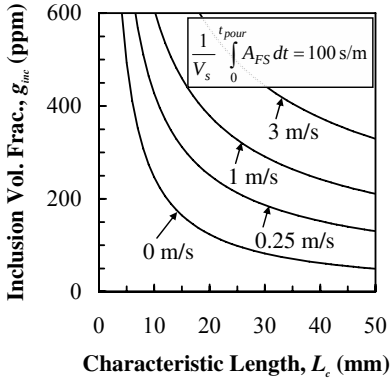

Figure 2. Variation of inclusion volume fraction with characteristic free surface length and melt surface velocity.

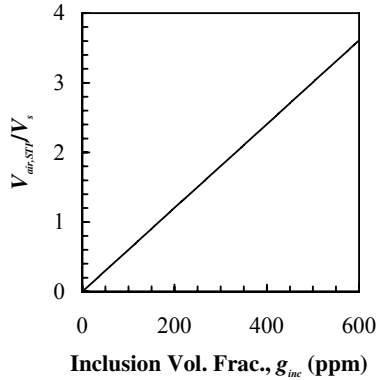

Figure 3. Variation of ambient air consumption with inclusion volume fraction.

The final inclusion locations are determined by tracking the motion of each inclusion from its nucleation until the end of filling. This is accomplished by solving the equation of motion, given in Equation (3), for each inclusion at each time step. Equation (3) accounts for both buoyancy and drag forces on each inclusion, where the drag is computed using the relative velocity between the inclusion and the surrounding melt. If an inclusion comes into contact with a mold wall, the inclusion is assumed to stick where it makes contact.

For typical production castings, simulating every inclusion in a casting quickly becomes computationally overwhelming. Typical aluminum-killed low alloy steel contains about 10^8 inclusions/kg [5], which gives an inclusion number density on the order of 10^{12} m^{-3}. With the present model, inclusion tracking is reasonable up to about 10^6 to 10^7 inclusions; beyond this, computational speed and storage become problematic issues. However, the vast majority of the 10^{12} m^{-3} inclusions are tiny. In continuous casting of steel, it has been found that only about 10^7 m^{-3} inclusions are larger than 80 microns, and the number larger than 200 microns is on the order of 10^4 m^{-3} [5]. In steel sand casting, the tiny (less than 80 microns) inclusions are not a concern in terms of surface quality. Although large in number, tiny inclusions make up a small percentage of the total inclusion volume. Furthermore, they lack buoyancy due to their small size, and are thus distributed relatively evenly throughout the casting. It is only the larger inclusions that are of interest here. The present model attempts to track the larger inclusions through the use of agglomeration, which is controlled through specification of the agglomeration length, L_{agg}. During each simulation time step, the agglomeration algorithm considers each inclusion, and finds all other inclusions whose centers are within the distance L_{agg} from the center of the inclusion under consideration. All inclusions within this distance are combined into a single, agglomerated inclusion, preserving overall inclusion volume and momentum. This model favors larger inclusions, neglecting the immense number of small inclusions by absorbing them into larger ones. It is emphasized that the actual physics of inclusion agglomeration are not considered in the present model. The primary goal of the agglomeration model is to make inclusion simulation computationally feasible by limiting the number of inclusions to a

manageable level, while preserving the total oxide volume and predicting reasonable sizes for the larger inclusions. The agglomeration length is considered an adjustable constant in this study. Note that in the present model, it would be pointless to have $L_{nuc} < L_{agg}$; inclusions would nucleate and then be agglomerated together in the same time step. Therefore, these parameters are taken to be the same, $L_{nuc} = L_{agg}$.

3. Experimental Inclusion Measurements

The foundry participating in this study provided experimental inclusion data in the form of concentration diagrams, which are part diagrams (showing all views of the casting) marked with the location of visible inclusions. Concentration diagrams were provided for 30 castings of each of the two casting geometries considered in this study. Note that the surfaces on the outer circumference of all castings were machined before concentration diagrams were created. All of the concentration diagrams provided were then digitized onto a solid model of the part, assigning a value of one to inclusions and a value of zero to areas without inclusions. For the large spindle shown in Fig. 4a, an example of a digitized concentration diagram (front view) is given in Fig. 4b, where the inclusions are indicated as dark areas on the casting. For each casting geometry, the digitized concentration diagrams were superimposed, summing the digitized values at each location on the casting surface and then dividing by the number of castings (30). This provides the probability (from 0 – 1) that an inclusion is present at a given point on the casting surface. The experimental inclusion probability distribution for the large spindle is shown in Fig. 4c.

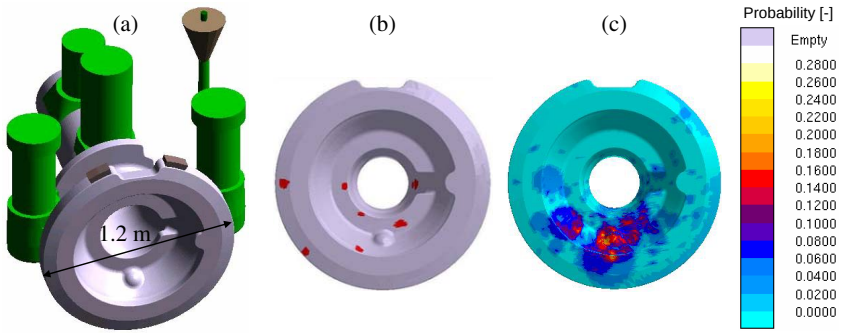

Figure 4. (a) Schematic of large spindle casting; (b) experimental inclusion distributions (inclusions are dark areas) for one casting, mapped onto a front view of the spindle; (c) experimental probability (based on 30 castings) of inclusions being present on the spindle

4. Comparison Between Simulation and Experiment

Filling simulations using the present inclusion model were performed for two different production carbon steel castings: a large spindle (3818 kg) and a small spindle (2432 kg). Both were cast in a phenolic urethane cold box (PUCB) mold, using a bottom-pour ladle. Casting data was collected for 30 castings of each geometry. The pouring temperature, time and head height used for the simulations were the average values of the 30 castings produced of each geometry.

For the large spindle shown in Fig. 4a, two inclusion simulations were performed; one with L_{agg} = 5 mm and one with L_{agg} = 10 mm. Fig. 5 shows the resulting inclusions for a simulation with L_{agg} = 10 mm at two different times during filling. The scale in this figure indicates the

inclusion diameter. As filling proceeds, inclusion sizes are seen to increase as inclusions grow. The L_{agg} = 5 mm simulation resulted in a total of 2.51×10^5 inclusions at the end of filling. Dividing the total number of inclusions by the casting volume ($0.474\,m^3$), the final inclusion number density is $5.3\times10^5\ m^{-3}$. The average inclusion diameter is 1.05 mm. The L_{agg} = 10 mm simulation resulted in 7.99×10^4 inclusions (inclusion number density $=1.7\times10^5\ m^{-3}$), with an average inclusion diameter of 1.54 mm. Both simulations resulted in a final inclusion volume fraction of 325 ppm. These numbers indicate that both simulations track a reasonable number of the larger inclusions that occur, and that the sizes of these inclusions are reasonable as well. In order to qualitatively compare these inclusion simulation results to the experimental inclusion probability result for this geometry (shown in Fig. 6a), inclusion area fraction plots were generated for the inclusion simulation results at the end of filling. This area fraction was determined by computing the total cross-sectional area of the inclusions at the casting surface in a region, and dividing that area by the total casting surface area in the region. The resulting inclusion area fraction results are shown for simulations run with agglomeration lengths L_{agg} = 5 mm (Fig. 6b) and L_{agg} = 10 mm (Fig. 6c). Comparing Figs. 6b and 6c, it is seen that the choice of agglomeration length in this range has a relatively small impact on the resulting inclusion area fraction distribution. Comparing both of these simulation results to the experimental result in Fig. 6a, the inclusion distributions in the simulations are seen to be in good agreement with the experimental results. In particular, the region with the highest probability of inclusions in Fig. 6a is seen to have high inclusion area fractions in Figs. 6b and 6c. Fig. 7 shows a comparison of the side views of the experimental result (Fig. 7a) and the simulation result for L_{agg} = 10 mm (Fig. 7b). The L_{agg} = 5 mm result is not included because it is very similar to the L_{agg} = 10 mm result. This view of the casting again shows reasonable agreement between simulation and experiment. Note that the simulation result shows most of the inclusions on the cope side of the casting; this is the result of the buoyancy of the inclusions lifting them to the cope surface during filling. The concentration on the cope surface in Fig. 7a is not as obvious, but the exterior of each spindle casting was machined prior to the creation of the concentration diagrams, so some cope surface inclusions may have been removed. The inside of the spindle, where the inclusions are concentrated in Fig. 6, was not machined. Note that the numbers on the scales in the experimental and simulation results in Figs. 6 and 7 cannot be directly compared: the experimental scale is the probability among 30 castings that an inclusion will exist at a particular location, whereas the simulation scale is the distribution of the local inclusion area fraction for the simulation performed with average casting conditions.

To examine more directly how well the measured and predicted results agree, the total inclusion area fractions on the casting surface were determined. The indication area fraction was obtained for each of the 30 inclusion maps (see Fig. 4b), by computing for each casting the total area containing inclusions (red areas) and dividing this area by the total casting surface area. The average indication area fraction for all 30 large spindle castings was found to be 0.76%. It is interesting to note that there was a large variation from casting to casting: the indication area fractions ranged from essentially 0% (no inclusions) up to 6.5%. Similarly, for the simulation results, the inclusion area fraction was computed over the entire casting. For L_{agg} = 5 mm (Fig. 6b), the inclusion area fraction was 0.91%, and for L_{agg} = 10 mm (Fig. 6c), the inclusion area fraction was 0.65%. These area fractions compare well with the experimental average value of 0.76%, and are they relatively close to each other, further emphasizing that this difference in agglomeration length is not important.

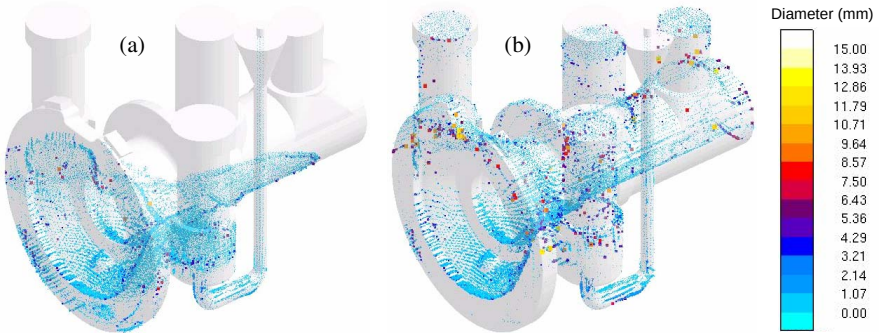

Figure 5. Simulation results with L_{agg} = 10 mm, showing inclusions generated during the filling sequence for the large spindle casting. The scale indicates the size of each inclusion

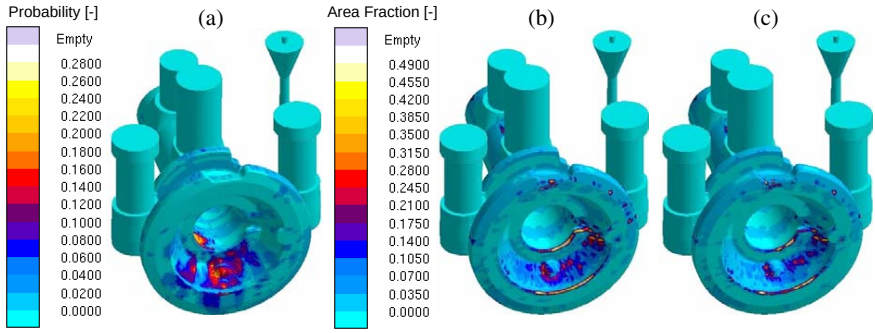

Figure 6. (a) Experimental inclusion probability plot for large spindle casting; along with inclusion area fraction simulation results using (b) L_{agg} = 5 mm and (c) L_{agg} = 10 mm.

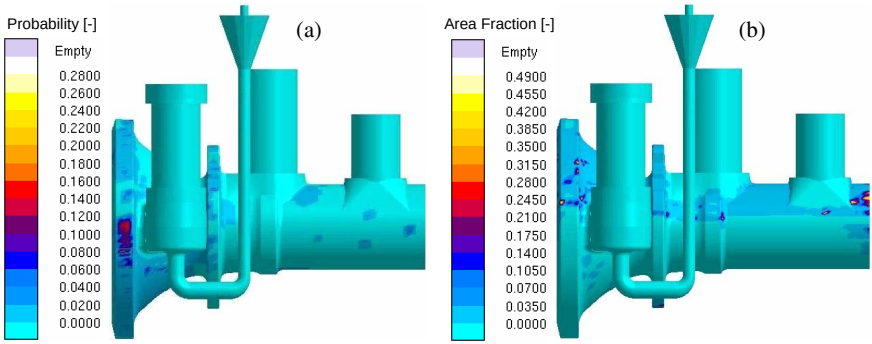

Figure 7. Large spindle casting side views of (a) experimental inclusion probability plot; and (b) inclusion area fraction simulation results using L_{agg} = 10 mm.

For the small spindle casting (see Fig. 8a), the experimental inclusion probability is given in Fig. 8b, and the simulated inclusion area fraction distribution is shown in Fig. 8c. An

agglomeration length of L_{agg} = 10 mm was selected for this simulation, based on the results for the large spindle. The small spindle simulation resulted in 9.73×10^4 inclusions (i.e., 2.6×10^5 m^{-3}), with an average inclusion diameter of 1.42 mm and a final inclusion volume fraction of 401 ppm. Good agreement is again seen between simulation and experimental results, particularly in the region in Fig. 8b with the highest probability of inclusions. The simulation correctly predicts a high inclusion area fraction in this region.

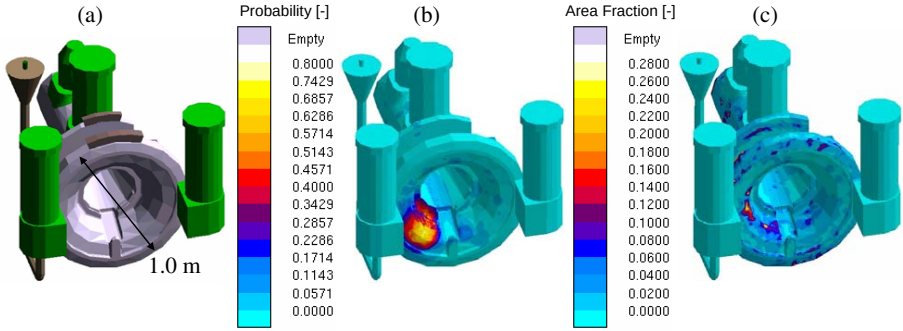

Figure 8. (a) Schematic of small spindle casting; (b) experimental inclusion probability plot; and (c) inclusion area fraction simulation results using L_{agg} = 10 mm.

5. Conclusions

A model for simulating the development and movement of reoxidation inclusions during pouring of C&LA steel sand castings has been developed that predicts the distribution of the inclusions on the casting surface. Parametric studies are performed to investigate the sensitivity of the predictions to model parameters. The model is validated by comparing the simulation results to inclusion measurements made on two production steel casting parts. Good agreement is seen between simulated and experimental inclusion distributions.

Acknowledgements

This work was supported by the Iowa Energy Center under grant number 06-01. The authors would like to thank Harrison Steel Castings Company and MAGMA GmbH for their generous support through the donation of software, time and information.

References

1. J.A Griffin and C.E. Bates, “Ladle Treating, Pouring and Gating for the Production of Clean Steel Castings,” Steel Founders' Society of America Research Report No. 104 (1991).

2. L. Wang and C. Beckermann, “Prediction of Reoxidation Inclusion Composition in Casting of Steel,” *Metall. Mater. Trans. B*, 37B (2006), 571-588.

3. *MAGMASOFT*, MAGMA GmbH, Kackerstrasse 11, 52072 Aachen, Germany.

4. A.J. Melendez, K.D. Carlson, and C. Beckermann, " Simulation of Reoxidation Inclusion Formation in Steel Casting,” (Paper presented at the 61st SFSA Technical and Operating Conference, Chicago, Illinois, December 2007).

5. L. Zhang and B.G. Thomas, “State of the Art in Evaluation and Control of Steel Cleanliness,” ISIJ Int., 43 (3) (2003), 271-291.